Chapter 0.1
GROUND PROBING RADAR

Michael Oristaglio, Douglas E. Miller, and Jakob Haldorsen
Schlumberger-Doll Research
Old Quarry Road
Ridgefield, CT 06877
USA

SCATTERING AND GPR

E-M GPR

Contents

0.1.1. Overview

"RADAR" is an acronym for "RAdio Detection And Ranging". In free space and in air (to a good approximtion), radio waves propagate at the speed of light—299,792,458 m/s or about .3 m/ns—and scatter from objects such as airplanes, ships, and clouds. By sending out pulses or bursts of radio waves from transmitting antennas and by detecting and timing the echoes returning to receiving antennas, we can accomplish the task escribed by the acronym. When the echoes come mainly from distant objects, i.e., from objects many wavelengths removed from the radar system, the same physical antenna can be used as both transmitter and receiver. Most radars operate at frequencies that lie in the RF and microwave bands, which cover the electromagnetic (EM) spectrum from roughly 300 kHz to 300 GHz. At these frequencies, the wavelength of EM waves in free space ranges from about 1 km to 1 mm, and the choice of operating frequency depends mainly on the size of the objects to be detected. Conventional radar has a vast literature: Skolnik (1980) is a standard technical reference; Buderi (1996) recounts the history of radar during the years leading into World War II.

"Ground probing radar" refers to the use of radio waves to detect and locate buried objects. Also called "ground-penetrating radar" or "GPR", directing radio waves into the ground is becoming a powerful way of mapping the shallow suburface in civil engineering, environmental studies, forensics, and archaeology. Versatile GPR systems ("GPRs"), consisting essentially of pairs of transmitting and receiver antennas with control electronics, are available from several commercial manufacturers; many more research systems have been developed for special uses, e.g., locating unexploded ordnance (UXO).

Figure 1 shows data obtained by scanning a GPR across a concrete floor with steel reinforcement that overlies an iron pipe. The horizontal scale is distance in meters giving the location of the radar antennas along a scan line on the floor. The vertical axis is recording time in nanoseconds. The echoes from the pipe for different positions of the antennas lie along the red line superimposed on the raw data. The locus of echoes has a hyperbolic shape characteristic of returns from small objects in homogeneous media. Because the speed of propagation is approximately .125 m/ns and the pipe is at approximately .5 m below the surface, the apex of the hyperbola occurs at approximately 8 ns.

Figure 1 Example of GPR data

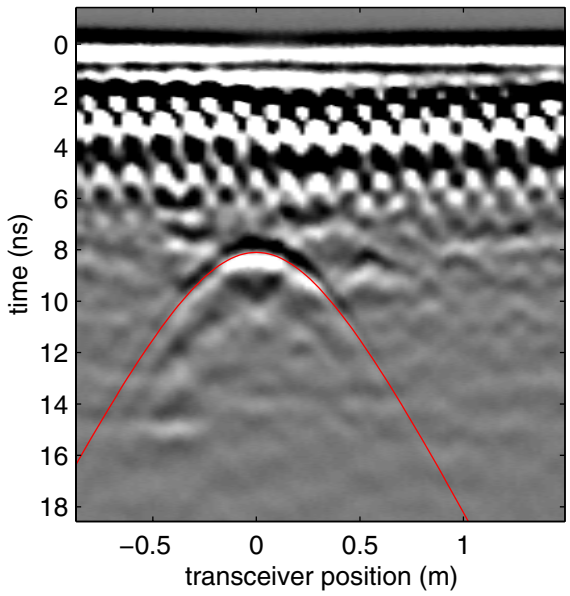

Figure 2 Example of 3D GPR image

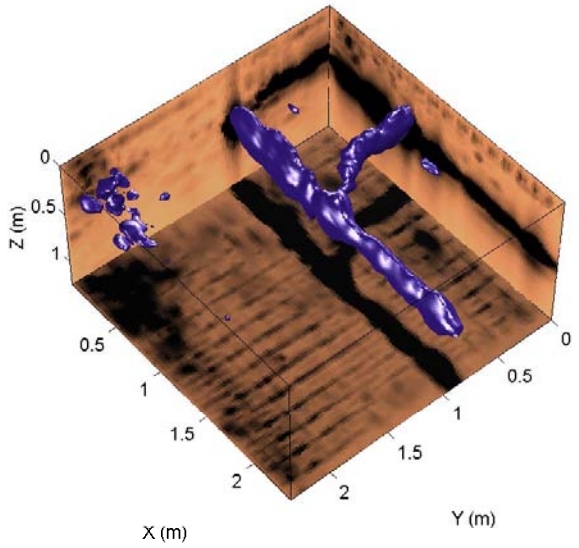

By moving the surface antennas over a regularly spaced grid of scan lines and processing the data with an imaging operator to be described below, it is possible to go beyond detection and ranging to make 3-D images similar to those made in X-ray tomography, magnetic-resonance imaging, medical ultrasound, and seismic exploration. Figure 2 shows a 3-D radar image of the pipe beneath the floor made from a dense set of scans which includes the one in Figure 1. It is natural to call this technique "ground-penetrating *imaging* radar" or "GP*i*R".

The sections that follow start with a conceptual and mathematical description of GPR, including the most useful analytical models of radar propagation in the ground and a simple, but rigorous, model of radar scattering which leads to a consistent formalism for 3D imaging. The article concludes with a brief description of practical GPR systems and examples of applications.

0.1.2. Conceptual Description

An Idealized GPR System

Figure 3 shows an idealized GPR system. It consists of one or more (polarized) transmitting antennas for broadcasting a short pulse of EM energy and one or more (polarized) receiving antennas for detecting the broadcast signals and their echoes. Control electronics generates the current pulse which excites the transmitting antenna and then samples and records the voltages at the receiving antennas. The EM wave from the transmitter propagates both in the air (direct wave) and in the earth, where it reflects off geological structures such as changes in soil layers or man-made objects before returning to the surface. The time of arrival of the echos is the principal source of information about buried structures.

Two features distinguish GPR from other radars. First, the antennas for transmitting and receiving GPR are roughly the same size as the spatial wavelengths of the propagating waves. Such antennas can be only weakly directional; therefore, precise location of a buried object with GPR requires synthetic-aperture focussing. Second, the speed of propagation in the ground is significantly different from the speed of light in free space and is not known *a priori*. Moreover, because most soils have finite conductivity when wet, the wavespeed is usually com-

Figure 3 Idealized GPR system

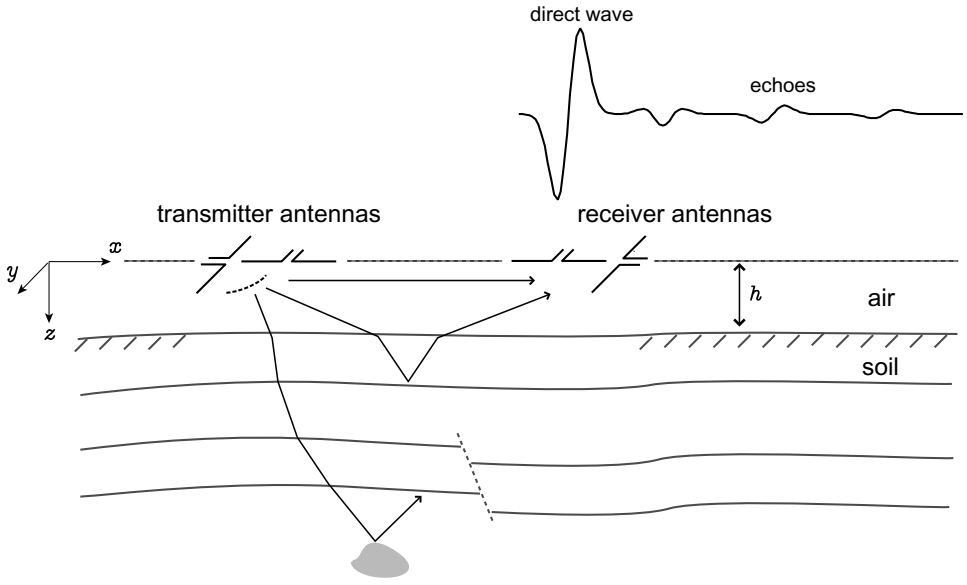

Figure 4 Electrical properties as a function of frequency for clay loams of Puerto Rico type with 2.5%, 5%, and 10% moisture content by weight (Hipp, 1974). Solid curves are experimental data; dotted curves are fits with a two-term Debye relaxation model (Wang and Oristaglio, 2000).

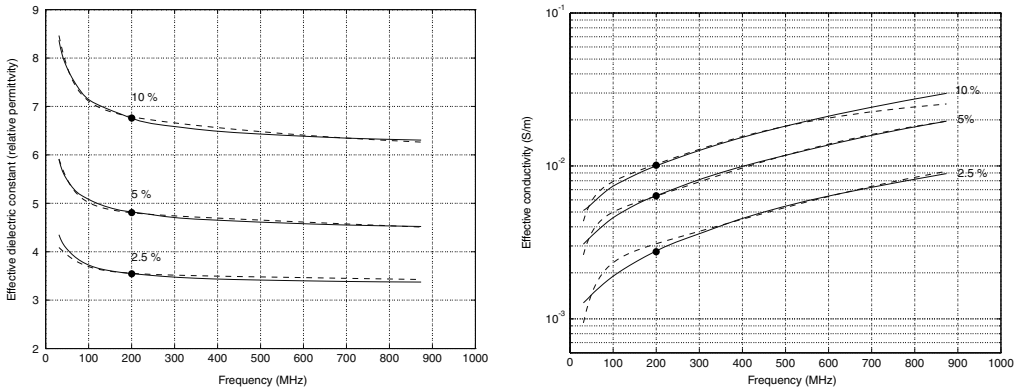

plex and varies moderately with frequency (Figure 4). A complex wavespeed (or propagation constant) means that the wave decays exponentially along its path of propagation; this limits severely the depth of penetration of radar signals in the ground.

Mathematical Description

GPRs generate and detect classical EM fields that are described by Maxwell's equations. To develop solutions relevant to GPR, we will use Cartesian coordinates with position vector $\mathbf{r} = x\hat{\mathbf{x}} + y\hat{\mathbf{y}} + z\hat{\mathbf{z}}$, where $\{\hat{\mathbf{x}}, \hat{\mathbf{y}}, \hat{\mathbf{z}}\}$ are unit vectors in the coordinate directions; $R = |\mathbf{r}| = \sqrt{x^2 + y^2 + z^2}$; and $\hat{\mathbf{r}} = \mathbf{r}/R$.

For fields varying harmonically in time as $\exp(-i\omega t)$, where ω is angular frequency, t is time, and $i = \sqrt{-1}$, Maxwell's equations for the electric field $\mathbf{E}$ and magnetic field $\mathbf{H}$ are

$$\nabla \times \mathbf{E} = i\omega\mu\mathbf{H}, \tag{1}$$

$$\nabla \times \mathbf{H} = -i\omega\epsilon\mathbf{E} + \sigma\mathbf{E} + \mathbf{J}_s. \tag{2}$$

where the source of the EM fields is represented by the impressed current density $\mathbf{J}_s$ (currents on the transmitting antenna), and the medium's EM properties are its permittivity ϵ, conductivity σ, and permeability μ. In the most general anisotropic medium, these properties are all tensor functions of frequency and position $(\mathbf{r}, \omega)$. We will assume for simplicity that electrical anisotropy is negligible and, morevoer, that μ assumes its free-space value $\mu_0 = 4\pi \times 10^{-7}$ H/m, which holds for many sandy and clay soils.

The important material properties for GPR are therefore the permittivity ϵ and conductivity σ, which determine the relative size of induced conduction ($\sigma\mathbf{E}$) and displacement ($-i\omega\epsilon\mathbf{E}$) currents in the ground. These secondary currents—and their variations caused by changes in soil or its pore fluids and by buried objects such as metallic pipe—generate the scattered EM fields that are detected by GPR. When both conduction and displacement currents are significant, it is convenient to combine them into a total (induced) current density,

$$\mathbf{J}_T = -i\omega\epsilon\mathbf{E} + \sigma\mathbf{E} = -i\omega(\epsilon + i\sigma/\omega)\mathbf{E} \tag{3}$$

and define the quantity in parenthesis as the complex permittivity,

$$\bar{\epsilon}(\omega) = \epsilon(\omega) + i\sigma(\omega)/\omega. \tag{4}$$

There is no loss of generality in then assuming that ϵ and σ are (strictly) real functions, linked by the requirement that

$$\bar{\epsilon}(t) = \frac{1}{2\pi}\int_{-\infty}^{\infty} \bar{\epsilon}(\omega)\exp(-i\omega t)d\omega$$

be a causal function of time. One convenience of this representation is that nearly all formulas derived for lossless media ($\sigma \equiv 0$) are extended to lossy media by the simple substitution $\epsilon \to \bar{\epsilon}$.

Finally is also conventional to write $\epsilon = \epsilon_0\epsilon_r$, where $\epsilon_0 = 8.85 \times 10^{-12}$ F/m is the permittivity of free-space and ϵ_r is the medium's relative permittivity, usually called its "dielectric constant". With these conventions, the speed of radio waves in the ground (at the operating frequencies of GPR) is determined mainly by $n = \sqrt{\epsilon_r}$, the index of refraction, while the attenuation is determined by both σ and n.

Propagation, Decay, and Dispersion Maxwell's equations (1) and (2) combine to give the vector wave equation,

$$\nabla \times \nabla \times \mathbf{E} - k^2(\omega)\mathbf{E} = i\omega\mu\mathbf{J}_s, \tag{5}$$

where $k^2 = \omega^2\mu\bar{\epsilon}(\omega)$. In regions outside the source, equation (5) has plane wave solutions of the form,

$$\mathbf{E}(\mathbf{r}, \omega) \sim \mathbf{E}_o\, e^{i\mathbf{k}\cdot\mathbf{r}}, \tag{6}$$

where $\mathbf{k}$ is a complex propagation vector and $\mathbf{E}_o$ is a complex amplitude vector, subject to

$$\mathbf{k}\cdot\mathbf{k} = k^2 = \omega^2\mu\bar{\epsilon}(\omega)\ ;\ \ \mathbf{E}_o\cdot\mathbf{k} = 0. \tag{7}$$

To simplify, assume the wave propagates along the z-axis, and is polarized along the y-direction; then

$$E_y(z,\omega) = E_o e^{ikz} \tag{8}$$

where

$$k = k_R + ik_I = \omega\sqrt{\mu\epsilon}\left(1 + i\frac{\sigma}{\omega\epsilon}\right)^{1/2} \tag{9}$$

is the wave's complex propagation constant and E_o is its (real) amplitude at the surface $z = 0$. In general, solution (8) describes a wave which propagates at phase velocity ω/k_R and decays at the rate k_I in the positive z-direction (when $k_R, k_I, \omega > 0$ and time-dependence $e^{-i\omega t}$ is restored). Solving for the complex square root shows that both the speed and attenuation depend on frequency, so that radar propagation in conductive soil is inherently dispersive, even if ϵ and σ are constant with frequency.

Dispersion can significantly complicate "detection and ranging" since it changes the shapes and locations of echoes. But its effects in GPR are not necessarily severe. Most GPRs operate at frequencies where displacement currents dominate, $\sigma/(\omega\epsilon) \ll 1$, and the propagation constant simplifies considerably

$$k \approx \omega\sqrt{\mu\epsilon}\left(1 + i\frac{\sigma}{2\omega\epsilon}\right) = \omega/c + i\alpha, \tag{10}$$

with

$$c = \frac{1}{\sqrt{\mu\epsilon}} = \frac{c_0}{n} \qquad \text{and} \qquad \alpha = \frac{\sigma}{2}\sqrt{\frac{\mu}{\epsilon}} = \frac{\eta_0\sigma}{2n}, \tag{11}$$

where $c_o = (\mu_0\epsilon_0)^{-1/2}$ is the speed of light in free-space, $n = \sqrt{\epsilon_r}$ is the index of refraction, and $\eta_0 = (\mu_0/\epsilon_0)^{1/2} \approx 377\ \Omega$ is the impedance of free-space. In this regime, the wavespeed and the attenuation rate are *independent of frequency* if ϵ and σ are constant. Pulses in this regime retain their shapes, but are attenuated exponentially along the path of propagation at a rate that is constant with frequency. Thus, when $\sigma/(\omega\epsilon) \ll 1$, a lower frequency GPR does not necessarily have increased depth of penetration. In practice, however, water in the soil does cause some variation of both ϵ and σ at frequencies in the bandwidth of GPR (Figure 4). The examples below show that this dispersion has only subtle effects on echoes from buried objects. But the higher attenuation caused by higher σ at higher frequencies can be significant.

Most soils have dielectric constants in the range 2-16, which means that speed of propagation in the ground is as much as four times slower than in air, and there is significant refraction of radio waves at the earth-air interface. Conductivity varies from nearly zero in dry sandy soils to about .1 S/m in wet clays. Both of these properties are influenced strongly by the amount of (salt) water saturation. (Values of conductivity are often given in terms of their inverse, the resistivity, $\rho = 1/\sigma$. Most soils have resistivities in the range 10–10 000 Ω-m.)

Antennas and Sources The most popular commercial GPRs use either linear or bow-tie antennas (Figure 5) backed by a metal cavity containing a radar-absorbing dielectric material. Modeling these in detail is complicated (Nishioka, et al., 1999), but their radiated fields are approximated well by that of an ideal (broadband) electric dipole. The induced secondary currents on a small isolated object also radiate, to good approximation, as an equivalent electric dipole (in the limit of an ideal point scatterer, this equivalence is exact).

Figure 5 GPR bow-tie antennas

Thus, the solution of the vector wave equation in a homogeneous medium where the source is a point electric dipole in an arbitary direction—i.e., $\mathbf{J}_s = \delta(\mathbf{r})\hat{\mathbf{u}}$—is probably the most important model in GPR.

We can obtain this solution from the Green's dyadic for the vector wave equation, which satisfies

$$\nabla\times\nabla\times\widetilde{\mathbf{G}}_o(\mathbf{r},\mathbf{r}',\omega) - \omega^2\mu\bar{\epsilon}\widetilde{\mathbf{G}}_o(\mathbf{r},\mathbf{r}',\omega) = \widetilde{\mathbf{I}}\,\delta(\mathbf{r}-\mathbf{r}'). \tag{12}$$

where $\widetilde{\mathbf{I}} = \hat{\mathbf{x}}\hat{\mathbf{x}}+\hat{\mathbf{y}}\hat{\mathbf{y}}+\hat{\mathbf{z}}\hat{\mathbf{z}}$ is the identity dyadic. Green's dyadic plays the role of Green's function for problems with vector fields and sources. If $\hat{\mathbf{u}}$ is a arbitrary unit vector, then

$$i\omega\mu\widetilde{\mathbf{G}}_o(\mathbf{r},\mathbf{r}',\omega)\cdot\hat{\mathbf{u}} \tag{13}$$

is the vector electric field at position $\mathbf{r}$ caused by a point electric dipole with unit strength and direction $\hat{\mathbf{u}}$ at position $\mathbf{r}'$. In Cartesian coordinates, Green's dyadic can be represented as a 3×3 matrix whose columns are (proportional to) the vector electric field caused, respectively, by electric dipoles in the coordinate directions $\hat{\mathbf{x}}$, $\hat{\mathbf{y}}$, and $\hat{\mathbf{z}}$. A dyadic (matrix) Green's function is needed because the field vector is not necessarily parallel to the source vector.

Green's dyadic for a homogeneous medium has a simple explicit form, that splits neatly into two terms,

$$\begin{aligned}\widetilde{\mathbf{G}}(\mathbf{r},\mathbf{r}',\omega) &= (\widetilde{\mathbf{I}} + k^{-2}\boldsymbol{\nabla}\boldsymbol{\nabla})\frac{e^{ikR}}{4\pi R} \\ &= (\widetilde{\mathbf{I}} - \hat{\mathbf{R}}\hat{\mathbf{R}})\frac{e^{ikR}}{4\pi R} \\ &+ \left(\frac{i}{kR} - \frac{1}{k^2R^2}\right)(\widetilde{\mathbf{I}} - 3\hat{\mathbf{R}}\hat{\mathbf{R}})\frac{e^{ikR}}{4\pi R}, \quad (14)\end{aligned}$$

where $R = |\mathbf{r} - \mathbf{r}'|$, $\hat{\mathbf{R}} = (\mathbf{r} - \mathbf{r}')/R$, and $k = \omega\sqrt{\mu\bar{\epsilon}}$. Positive real and imaginary parts are chosen for the square root to give an outgoing and decaying spherical wave, with $\exp(-i\omega t)$ time-dependence. The first term, which dominates at large distances compared to a wavelength ($|kR| = 2\pi R/\lambda \gg 1$) is the radiation or far field. The dyadic factor in this term guarantees that its electric field is polarized perpendicular to the direction of propagation (the radial vector from the source). The radiation field thus locally resembles an EM plane wave. The polarization of the near-field (second) term is the same as that of a static electric dipole.

The transient field of the dipole is, from (13) and (14),

$$\mathbf{E}(\mathbf{r},t) = Re\left\{\frac{\mu}{\pi}\int_0^\infty i\omega\widetilde{\mathbf{G}}(\mathbf{r},\mathbf{r}',\omega)\cdot\mathbf{J}(\mathbf{r}',\omega)e^{-i\omega t}d\omega\right\}. \quad (15)$$

In conductive media, the integral must be evaluated numerically, but it simplifies considerably when $\sigma = 0$. If $I(\omega)$ is the dipole's current moment (in units of amp-m) so that $\mathbf{J} = I(\omega)\delta(\mathbf{r} - \mathbf{r}')\hat{\mathbf{u}}$, then in the far field, the transient electric field is just the time-derivative of the current waveform with the propagation delay R/c,

$$\mathbf{E}(\mathbf{r},t) \approx (\widetilde{\mathbf{I}} - \hat{\mathbf{R}}\hat{\mathbf{R}})\cdot\hat{\mathbf{u}}\,\frac{\mu}{4\pi R}I'(t - R/c), \quad (R \to \infty) \quad (16)$$

where $I' = dI/dt$. The time-dependence of the near-field term includes a combination of the source current and its integral.

In conductive soil, the wave is attenuated and distorted significantly as it propagates, but in soils where $\omega\epsilon/\sigma \gg 1$ in the effective bandwidth of the source current, the main effect in the far field is an exponential attenuation,

$$\mathbf{E}(\mathbf{r},t) \approx (\widetilde{\mathbf{I}} - \hat{\mathbf{R}}\hat{\mathbf{R}})\cdot\hat{\mathbf{u}}\frac{\mu e^{-\alpha R}}{4\pi R}I'(t - R/c), \quad (R \to \infty) \quad (17)$$

where $\alpha = \sigma\mu c/2 = \sigma\eta_0/(2n)$.

Figure 6 shows the evolution from the near to far field in a wholespace with relative dielectric $\epsilon_r = 9$, a typical value for sandy soils, corresponding to a speed of light of .1 m/ns. Waveforms are shown for soils in which the conductivity increases from 0 to .05 S/m (a relatively conductive soil). The source current is the first derivative of a gaussian function with a central frequency of about 200 MHz. The wavelength in the non-conductive soil at the central frequency of the source is about 0.5 m. At a distance of 1.5 m from the source—or 3 wavelengths at the central frequency—the far field approximation is already accurate to a few per cent.

Earth-Air Interface Presence of the interface between earth and air is another obvious difference between GPR and conventional radar. Sommerfeld (1912) began the study of radio waves near the interface by constructing his famous integral, and exploration of its subtleties remains an area of active research (e.g., to determine where cellular phones will work). Fortunately, when GPR antennas are placed close to the ground—within a quarter wavelength or less, as in most surveys—most of these subtleties can be ignored. The main effect of the interface on scattering by buried objects is a change in the radiation and receiving patterns of the antennas. This effect is accurately modeled by asymptotic formulas for Green's dyadic in a halfspace. For GPR surveys with horizontal antennas on the ground, the relevant components of Green's dyadic—the first 2 columns, corresponding to the (vector) electric fields in the halfspace caused by x- and y-directed dipoles at the interface—can be obtained from the formulas for the field of a horizontal dipole at the interface (Engheta et al., 1982). The solution is conviently written with the dipole at the origin in spherical coordinates,

$$\widetilde{\mathbf{G}}(\mathbf{r},\mathbf{r}'=0) \sim \frac{e^{-\sigma\mu cR}}{4\pi R}e^{i\omega R/c}\left[F(\theta)\hat{\boldsymbol{\phi}}\hat{\boldsymbol{\phi}} - G(\theta)\hat{\boldsymbol{\theta}}(\hat{\boldsymbol{\phi}}\times\hat{\mathbf{z}})\right] \quad (18)$$

where θ and ϕ are polar and azimuthal angles of the radius vector to point $\mathbf{r}$; $\hat{\boldsymbol{\theta}}$ and $\hat{\boldsymbol{\phi}}$ are unit vectors in the corresponding directions; and the angular factors are

$$F(\theta) = \frac{2n\cos\theta}{(1 - n^2\sin^2\theta)^{1/2} + n\cos\theta} \quad (19)$$

$$G(\theta) = \frac{2n\cos\theta}{n(1 - n^2\sin^2\theta)^{1/2} + \cos\theta}(1 - n^2\sin^2\theta)^{1/2}, \quad (20)$$

where $n = \sqrt{\epsilon_r}$ is the index of the refraction of the ground.

GPR antennas close to the interface also excite a strong ground wave, which propagates at the speed of radar waves in the soil. Thus, GPR data has two "direct" waves between transmitter and receiver antennas: one propagating in air and one in ground. These waves interfere when the two antennas are close together (within a wavelength or two), but separate clearly in any GPR survey in which the transmitter antenna is held fixed and the receiver is moved to successive larger separations or receivers are laid out in an array at different distances from the source.

Figure 7 Geometry of finite-difference calculation of scattering from a pipe in soil.

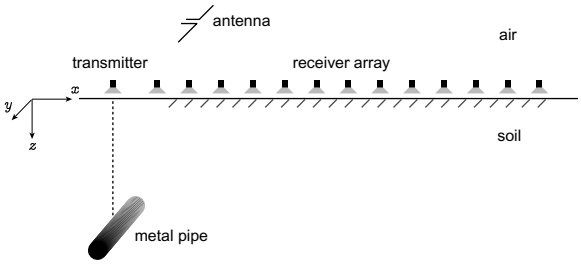

Example: Scattering from a pipe in soil

Models more complicated than a halfspace generally require a numerical solution. The popular finite-difference time-domain (FDTD) method for solving Maxwell's equations in 3D is easily adapted to GPR models and can include the effects of propagation in dispersive soils (Luebbers et al., 1990; Wang and Oristaglio, 2000).

Figure 8 shows synthetic waveforms for an experiment with geometry of Figure 7. Coherent events visible in the data include an air-coupled wave [A], a ground-coupled wave [G], and a wave scattered from the pipe [S]. The first two panels show the result, at low and high gain, when soil conductivity and permittivity are constant with frequency with the values indicated by the dots on the top curves in Figure 4. The third panel displays the waveforms at high gain for a dispersive soil in which the electrical parameters follow the dotted curves in Figure 4, which comes from a two-term Debye model that fits the properties of clay-loams of 10% moisture content (Hipp, 1974). The change in soil has little effect on the airwave, some effect on the phase of the ground and scattered waves, and a negligible effect on the propagation speed of the ground and scattered waves.

Figure 6 Evolution of transient field of a dipole in homogeneous conductive media. Center panel shows fields in freespace at distances (m) shown at left. Top and bottom panels show the fields in homogeneous wholespace of 100 and 20 ohm-m, respectively. Amplitudes are normalized by trace.

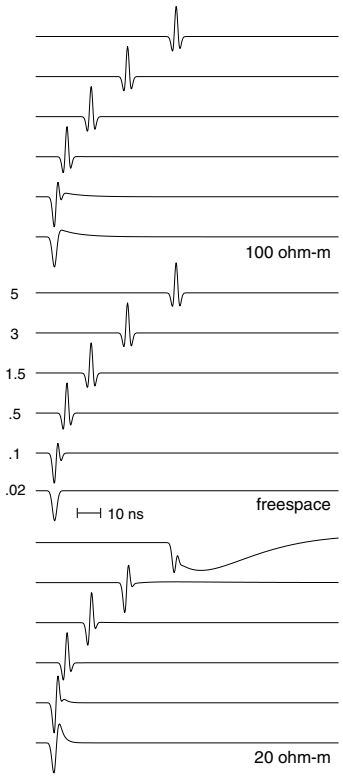

0.1.3. Location and Imaging with GPR

Conventional radars use directional antennas (or antenna arrays) to locate objects. These systems can broadcast a radar wave along a specific direction—i.e., within a certain angular spread—and time the echo returning to the same (physical) antenna (top of Figure 9). If t_e is the round-trip echo time, the object is located at radial distance (range) $ct_e/2$ from the antenna along the radar's "line of sight", which sweeps periodically through different directions. A fundamental result of antenna theory is that the angular spread of the main lobe of a broadcast wave is inversely proportional to the antenna's size in wavelengths (see, e.g., Kraus, 1988),

$$\Delta\Omega \sim 2\lambda/L. \tag{21}$$

This relationship sets the minimum size of an antenna designed to achieve a given angular resolution. Antenna size alone, of course, does not give directionality; it is also necessary to control the current pattern on the antenna by giving it a special shape or by controlling its individual elements. Neither of these options is very practical with a general-purpose GPR, which needs to move easily over the ground and to operate over soils with different wavespeeds (and therefore wavelengths).

It is nevertheless possible to achieve high resolution with a GPR by synthetically forming an image

Figure 8 Radargrams from pipe in model of non-dispersive and dispersive clay-loams of 10% moisture content.

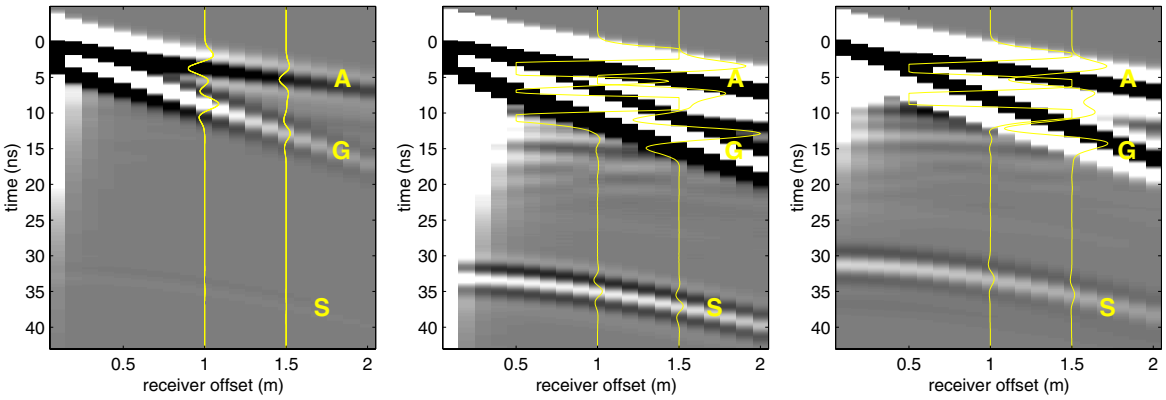

from data collected at different source and receiver positions with omni-directional antennas. This processing resembles conventional "synthetic-aperture radar" (SAR), in which an antenna array is synthesized by applying coherent phase delays to data obtained at different antenna positions. Before considering these imaging methods in detail, it is useful first to see how simple geometric ideas can be used to locate objects with GPR.

Geometry of Scattering

The arrival times of echoes recorded at different positions can easily be used to locate an object with non-directional radar if the object is small compared to the radar's wavelength. The simplest case is a pointlike object which scatters radar energy in all directions. Let $\mathbf{r}_p = (x_p, y_p, z_p)$ be the location of the point scatterer, while $\mathbf{r}_i$ and $\mathbf{r}_j$ are locations of the transmitting and receiving antennas, respectively. The equation for the arrival times of echoes from the point scatterer is

$$t_p = \frac{|\mathbf{r}_p - \mathbf{r}_i|}{c} + \frac{|\mathbf{r}_j - \mathbf{r}_p|}{c} \tag{22}$$

where c is the radar velocity (assumed to be constant). For simplicity, let the point scatterer be located in the (x, z) plane at $\mathbf{r}_p = (x_p, 0, z_p)$, and consider a standard GPR survey in which one transmitter and and one receiver, located at essentially the same position $\mathbf{r}_i \approx \mathbf{r}_j$, move together along a line (e.g., the x-axis) at the surface $z = 0$ above the scatterer (Figure 9). The curve of arrival times is then a hyperbola, such as the one we have overlain on the data of Figure 1,

$$t_p = 2\frac{\sqrt{(x_j - x_p)^2 + z_p^2}}{c}, \text{ or} \tag{23}$$

$$c^2 t_p^2 - 4(x_j - x_p)^2 = c^2 t_o^2 \tag{24}$$

where $t_o = 2z_p/c$ is the earliest arrival time, when the antenna pair is directly above the point scatterer.

The velocity c can be determined from the slope of the curve of echoes at large offsets,

$$\frac{dt_p}{dx} = \frac{2}{c}\frac{x - x_p}{\sqrt{(x_j - x_p)^2 + z_p^2}} \to \frac{2}{c} \quad (x_j \to \infty). \tag{25}$$

The horizontal location of the pipe is determined by the apex of the hyperbola $dt_p/dx = 0$; its depth is $z_p = ct_o/2$. These quantities could also be determined by fitting the locus of arrival times with the hyperbola (24).

A related way of looking at the problem of locating an object from its radar echoes is to see what can be learned from a single echo. If x_p and t_p are held fixed in equation (22), and if the velocity is known, then this equation determines the locus of possible scatterer positions $\mathbf{r}_p$ that could generate an echo arriving at the right time. The appropriate locus is clearly an ellipse (or ellipsoid in 3 dimensions) with the source and receiver antennas at the focus. If we assume the echoes are coming from an object in the ground, the ellipse becomes a semi-ellipse. When source and receiver are co-incident, this semi-ellipse becomes a semi-circle centered on the source-receiver pair, as given by (23), viewed as an equation for (x_p, z_p), with t_p and c fixed. A point scatterer located in the ground at any point along the semi-circle generates an echo at time t_p. This ambiguity in the object's position is inherent in any omni-directional radar operating at a fixed location; it is removed by considering semi-circles of possible scatterer positions corresponding to echoes received at other locations of the radar. All the semi-circles determined by times that satisfy equation (24) interesect at the point (x_p, z_p).

Synthetic Aperature Radar The hyperbolas and ellipses generated by equations 22 or 24 provide complementary pictures of radar echo location (with

non-directional antennas). One determines the locus of echoes that are generated by scattering from a single (point-like) object; the other generates the locus of object positions determined by a single echo. The geometry of these equations has inspired numerous algorithms that transform raw radar data into maps (or images) of object positions. One class of such algorithms, called Synthetic Aperture Radar or "SAR", computes a likelihood map of object positions by summing the data along travel-time curves. Let $D(ij,t)$ stand for the amplitude of the radar data at time t when the source is at position $\mathbf{r}_i$ and the receiver at position $\mathbf{r}_j$, and let $\mathbf{r}_p$ stand for a generic object position. Then, the value of a SAR likelihood map, or SAR image, at $\mathbf{r}_p$ is given by a summation of the form,

$$SAR(p) \equiv SAR(\mathbf{r}_p) = \sum_{ij} w(p,ij)\, D(ij, t(i,p,j)), \quad (26)$$

where $t(i,p,j)$ is total radar traveltime from source to point $\mathbf{r}_p$ and back to the receiver, and $w(p,ij)$ is a weighting function tailored to normalize amplitudes for different distances to the object position, polarization of the antennas, etc. The sum is computed for all possible object positions $\mathbf{r}_p$ and plotted in 2D or 3D.

The SAR formula is intuitively very appealing. If a (point-like) object is present at point $\mathbf{r}_p$, summing the data along the travel-time curve will add its echoes together coherently giving a large number, whereas random noise and interfering echoes from other objects will tend to add incoherently and cancel. The SAR formula can also be interpreted as a synthetic focussing—also called "phasing" or "steering"—of the array of receivers onto individual image points. Similar algorithms have been used in acoustic imaging for medical ultrasound and for geophysical exploration (where they are called "seismic migration", Claerbout, 1976). These heuristic interpretations can be made rigorous by using a consistent model of radar scattering.

Scattering Model for GPR Imaging

The Born approximation to electromagnetic scattering provides a simple (linear) scattering model that leads to a rigorous formulation of GPR imaging. In this model, the complex permittivity is first split into a background term $\bar{\epsilon}_o$ plus a perturbation $\delta\bar{\epsilon}$, both of which can vary spatially,

$$\bar{\epsilon}(\mathbf{r}) = \bar{\epsilon}_o(\mathbf{r}) + \delta\bar{\epsilon}(\mathbf{r}) \quad (27)$$

$$= \epsilon_o(\mathbf{r}) + \delta\epsilon(\mathbf{r}) + i\left[\sigma_o(\mathbf{r}) + \delta\sigma(\mathbf{r})\right]/\omega. \quad (28)$$

The background model represents the properties of the soil, which are taken to be known or are guessed; in practice, the background model is usually a homogeneous wholespace or halfspace. "Scattered waves" (i.e., radar echoes) are caused by the deviations $\delta\bar{\epsilon}$, which is an unknown 3-D function to be recovered by the imaging formula.

The approximate scattering model follows from the integral formula that represents the total electric field as the sum of the field in the background medium plus the scattered field. This formula uses Green's dyadics for the total field and the field in the background medium. The dyadic for the total field is the solution of the vector wave equation in the full medium with all variations in the properties of the soil and buried objects,

$$\nabla\times\nabla\times\widetilde{\mathbf{G}}(\mathbf{r},\mathbf{r}',\omega) - \omega^2\mu\bar{\epsilon}(\mathbf{r})\widetilde{\mathbf{G}}(\mathbf{r},\mathbf{r}',\omega) = \widetilde{\mathbf{I}}\,\delta(\mathbf{r}-\mathbf{r}'). \quad (29)$$

The dyadic for the background medium $\widetilde{\mathbf{G}}_o$ satisfies the vector wave equation in the background medium,

$$\nabla\times\nabla\times\widetilde{\mathbf{G}}_o(\mathbf{r},\mathbf{r}',\omega) - \omega^2\mu\bar{\epsilon}_o(\mathbf{r})\widetilde{\mathbf{G}}_o(\mathbf{r},\mathbf{r}',\omega) = \widetilde{\mathbf{I}}\,\delta(\mathbf{r}-\mathbf{r}'). \quad (30)$$

Figure 9 Synthetic aperture GPR: (Left) Hyperbola of arrival times of echoes from a point-like object in the ground as a transmitter-receiver pair is scanned along the surface. (Right) Ellipse of possible scatterer positions determined by a single echo. Dark curve corresponds to the antenna pair shown; light curves are for nearby positions.

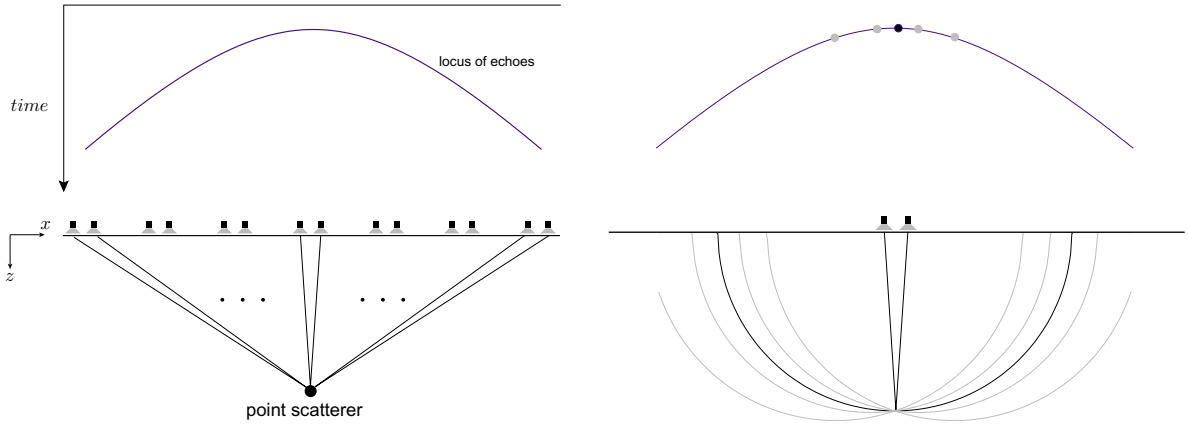

These Green's dyadics have the usual interpretation: if $\hat{\mathbf{u}}$ is a unit vector giving the direction of a dipole source at position $\mathbf{r}'$, then $i\omega\mu\widetilde{\mathbf{G}}(\mathbf{r},\mathbf{r}',\omega)\cdot\hat{\mathbf{u}}$ is the vector electric field at position $\mathbf{r}$ in the full medium; and $i\omega\mu\widetilde{\mathbf{G}}_o(\mathbf{r},\mathbf{r}',\omega)\cdot\hat{\mathbf{u}}$ is the vector electric field in the background medium.

We will assume that the transmitting antenna is an ideal electric dipole,

$$\mathbf{J}_s(\mathbf{r}) = I(\omega)\,\delta(\mathbf{r}-\mathbf{r}_j)\hat{\mathbf{u}}_j, \tag{31}$$

with current moment $I(\omega)$ (amp-m) and direction $\hat{\mathbf{u}}_j$, and that the output of the receiving antenna can be converted into a measurement of the electric field. These assumptions imply that radar data are essentially different components of the Green's dyadic. For example, with a GPR transmitter antenna aligned in the x-direction at position $\mathbf{r}_j$ and a receiver antenna aligned in the y-direction at $\mathbf{r}_i$ (a cross-polarized measurement), then the measured electric field is

$$i\omega\mu I(\omega)\;\hat{\mathbf{y}}\cdot\widetilde{\mathbf{G}}(\mathbf{r}_i,\mathbf{r}_j,\omega)\cdot\hat{\mathbf{x}}.$$

The measurement includes both the "direct" waves in the background medium and the EM field scattered by buried objects. When using radar to image the objects, one usually subtracts an estimate of the direct coupling between the transmitter and receiver antennas in the background medium. To model this, we use the "scattered field" dyadic, defined as the difference between the total field and the background field,

$$\widetilde{\mathbf{G}}_s(\mathbf{r},\mathbf{r}_j,\omega) \equiv \widetilde{\mathbf{G}}(\mathbf{r},\mathbf{r}_j,\omega) - \widetilde{\mathbf{G}}_o(\mathbf{r},\mathbf{r}_j,\omega). \tag{32}$$

A full set of scattered-field radar measurements then comprise a 3×3 data matrix,

$$\widetilde{\mathbf{D}}(\mathbf{r}_i,\mathbf{r}_j,\omega) = \begin{pmatrix} D_{xx} & D_{xy} & D_{xz} \\ D_{yx} & D_{yy} & D_{yz} \\ D_{zx} & D_{zy} & D_{zz} \end{pmatrix}, \tag{33}$$

where

$$D_{yx} = i\omega\mu I(\omega)\;\hat{\mathbf{y}}\cdot\widetilde{\mathbf{G}}_s(\mathbf{r}_i,\mathbf{r}_j,\omega)\cdot\hat{\mathbf{x}},\ \text{etc.} \tag{34}$$

With ideal dipoles as transmitters and receivers, the data matrix is symmetric because of reciprocity. Generally, only horizontal antennas are used in GPR surveys; this gives 3 independent polarizations from the upper-left 2×2 matrix: D_{xx}, D_{yy}, and $D_{xy} = D_{yx}$. In what follows, we maintain the convention that $\mathbf{r}_j$ represents positions of a transmitter antenna and $\mathbf{r}_i$ positions of a receiver antenna, and will refer to the Green's dyadics as "fields", since field components are obtained by sandwiching the dyadics with unit vectors and multiplying by $i\omega\mu I(\omega)$.

With these definitions, the scattered field has the integral representation,

$$\widetilde{\mathbf{G}}_s(\mathbf{r},\mathbf{r}_j,\omega) = \omega^2\mu\int_{V_s} d\mathbf{r}'\,\widetilde{\mathbf{G}}_o(\mathbf{r},\mathbf{r}',\omega)\cdot\widetilde{\mathbf{G}}(\mathbf{r}',\mathbf{r}_j,\omega)\delta\bar{\epsilon}(\mathbf{r}'), \tag{35}$$

in which the scattering currents, $(-i\omega\delta\bar{\epsilon})(i\omega\mu\widetilde{\mathbf{G}})$, driven by the total electric field in the scatterer, radiate with the background Green's dyadic. Equation (35) is the basic integral equation for forward and inverse EM scattering. The integration is over the region of support of the contrast function: $V_s = \{\mathbf{r}' : \delta\bar{\epsilon}(\mathbf{r}') \neq 0\}$. The point $\mathbf{r}$ where the field is computed can be anywhere. When the contrast function is known, equation (35) becomes a linear integral equation for the field by letting $\mathbf{r}$ range over the scattering region. When contrast function is unknown, as in radar imaging, equation (35) becomes a nonlinear integral equation for determining $\delta\bar{\epsilon}$ from the scattered field recorded outside the scattering region, $\mathbf{r} = \mathbf{r}_i \notin V_s$.

Inversion for $\delta\bar{\epsilon}$ is nonlinear because the total field $\widetilde{\mathbf{G}}$ which multiples $\delta\bar{\epsilon}$ in equation (35) also depends on $\delta\bar{\epsilon}$. The equation is linearized by replacing the total field $\widetilde{\mathbf{G}}$ in the integral by the background field $\widetilde{\mathbf{G}}_o$, giving

$$\begin{aligned}\widetilde{\mathbf{G}}_s^B(\mathbf{r}_i,\mathbf{r}_j,\omega) &= \omega^2\mu\int_{V_s} d\mathbf{r}'\,\widetilde{\mathbf{G}}_o(\mathbf{r}_i,\mathbf{r}',\omega)\cdot\widetilde{\mathbf{G}}_o(\mathbf{r}',\mathbf{r}_j,\omega)\delta\bar{\epsilon}(\mathbf{r}') &(36)\\ &= \omega^2\mu\int_{V_s} d\mathbf{r}'\,\widetilde{\mathbf{G}}_o^T(\mathbf{r}',\mathbf{r}_i,\omega)\cdot\widetilde{\mathbf{G}}_o(\mathbf{r}',\mathbf{r}_j,\omega)\delta\bar{\epsilon}(\mathbf{r}'). &(37)\end{aligned}$$

The second equation, which is perfectly symmetric in sources and receivers, follows from the symmetry of electric Green's dyadic under (matrix) transposition, $\widetilde{\mathbf{G}}^T = \widetilde{\mathbf{G}}$ (see, e.g., Felsen and Marcuvitz, 1975).

Equation (36) is the Born approximation for vector EM scattering (Chew, 1990). It is the only self-consistent linear relation between the scattered field and the perturbation $\delta\bar{\epsilon}$. All linear radar imaging methods therefore rest, explicitly or implicitly, on the assumption that this equation accurately models the actual scattered field—i.e., measured radargrams with the direct field substracted.[1] The next section develops a specific and flexible formula that is based on interpreting equation (36) as a generalized Radon transfrom. To simplify the notation in what follows, we will drop the superscripts "B" and "o" since everything relies on the Born approximation and the background model is the only model used in imaging.

EM Scattering as a Generalized Radon Transform

Quantitative radar imaging requires an inversion of equation (36) to recover $\delta\bar{\epsilon}$. A general theory for inverting this and similar equations, involving the Green's function of wave propagation, can be derived from the theory of Fourier Integral Operators (Beylkin, 1985) and the generalized Radon transform (Miller et al., 1987). The ordinary Radon transform is an operator that maps a function into its integrals over straight lines in 2D or planes in 3D. Its inverse is known explictly and provides the inversion formulas for X-ray tomography and magnetic resonance imaging (Deans, 1982). The generalized Radon transform (GRT) maps a function into its weighted integrals over a family of curved surfaces. Although the GRT is invertible under general conditions, explicity formulas exist only for specialized surfaces—such as for integrals over spheres (Helgason, 1984).

Putting equation (36) into the form of a GRT requires a further approximation that replaces the background Green's dyadic with its high-frequency approximation by geometrical ray theory. Since the development of this approximation for EM fields is lengthy, we will simply quote the relevant results. Details can be found in Born and Wolf (1983), Kline and Kay (1965), and Felsen and Marcuvitz (1973).

Geometrical ray theory assumes that the Green's dyadic in the high-frequency limit can be written as the product of a geometrical amplitude factor and an exponential (phase) factor:

$$\widetilde{\mathbf{G}}(\mathbf{r},\mathbf{r}') = \widetilde{\mathbf{A}}(\mathbf{r},\mathbf{r}')\ e^{i\omega\tau(\mathbf{r},\mathbf{r}')}, \tag{38}$$

where $\widetilde{\mathbf{A}}$ is a dyadic amplitude, independent of frequency, and $i\omega\tau$ is the phase. In this representation, τ will become the traveltime along a raypath. Equations for the amplitude and traveltime are developed by substituting equation (38) into (30) and taking the limit $\omega \to \infty$. The leading-order result is the eikonal equation for the traveltime,

$$\nabla\tau \cdot \nabla\tau = \mu\epsilon(\mathbf{r}). \tag{39}$$

and the transport equation for the dyadic amplitude (outside the source region),

$$\widetilde{\mathbf{A}}\nabla^2\tau + 2\nabla\tau\ \widetilde{\mathbf{A}} \cdot \nabla \ln \epsilon(\mathbf{r}) + 2(\nabla\tau \cdot \nabla)\widetilde{\mathbf{A}} + \sigma\mu\widetilde{\mathbf{A}} = 0, \tag{40}$$

where $\epsilon(\mathbf{r})$ and $\sigma(\mathbf{r})$ are the real permittivity and conductivity. When equations (39-40) are solved in the usual way—e.g., by tracing bundles of rays—the last term in equation (40) gives an additional exponential attenuation of the amplitude,

$$\exp\left(-\frac{1}{2}\int dl\ \sigma(\mathbf{r})\mu c(\mathbf{r})\right) \equiv \exp\left(-\int dl\ \alpha(\mathbf{r})\right), \tag{41}$$

where $\alpha(\mathbf{r})$ is the attenuation rate and the integral is along the raypath (Kline and Kay, 1965). For example, geometrical ray theory for a point dipole in a homogeneous conducting medium gives

$$\widetilde{\mathbf{G}}(\mathbf{r},\mathbf{r}') \sim (\widetilde{\mathbf{I}} - \hat{\mathbf{R}}\hat{\mathbf{R}})\frac{e^{-\alpha R}}{4\pi R}\ e^{i\omega R/c}, \tag{42}$$

which is just the far-field term in equation (14), with the further approximation that $\sigma/(\omega\epsilon) \ll 1$. As discussed before, the exponential attenuation in this regime is independent of frequency and is proportional to the product of the conductivity and the intrinsic impedance of the medium, $\eta = \sqrt{\mu/\epsilon}$.

Replacing the Green's dyadics in equation (36) with their asymptotic forms gives

$$\widetilde{\mathbf{G}}_s(\mathbf{r}_i,\mathbf{r}_j,\omega) = \omega^2\mu \int d\mathbf{r}'\ \widetilde{\mathbf{A}}(\mathbf{r}_i,\mathbf{r}',\mathbf{r}_j)\ e^{i\omega\tau(\mathbf{r}_i,\mathbf{r}',\mathbf{r}_j)}\ \delta\bar{\epsilon}(\mathbf{r}'). \tag{43}$$

where

$$\widetilde{\mathbf{A}}(\mathbf{r}_i,\mathbf{r}',\mathbf{r}_j) = \widetilde{\mathbf{A}}(\mathbf{r}_i,\mathbf{r}') \cdot \widetilde{\mathbf{A}}(\mathbf{r}',\mathbf{r}_j) \quad \text{and} \tag{44}$$

$$\tau(\mathbf{r}_i,\mathbf{r}',\mathbf{r}_j) = \tau(\mathbf{r}_i,\mathbf{r}') + \tau(\mathbf{r}',\mathbf{r}_j) \tag{45}$$

are the total amplitude and total traveltime along the path from source to scattering point to receiver. When transformed to the time domain, this equation becomes a generalized Radon transform in the time-domain. Consider, for example, the D_{yx} component of the data at time t,

$$D_{yx}(\mathbf{r}_i,\mathbf{r}_j,t) = \mu \int_{-\infty}^{\infty} d\omega e^{-i\omega t} i\omega^3 I(\omega) \cdot \int d\mathbf{r}'\ \hat{\mathbf{y}} \cdot \widetilde{\mathbf{A}}(\mathbf{r}_i,\mathbf{r}',\mathbf{r}_j) \cdot \hat{\mathbf{x}}\ e^{i\omega\tau(\mathbf{r}_i,\mathbf{r}',\mathbf{r}_j)}\ \bar{\epsilon}(\mathbf{r}') \tag{46}$$

$$= -\mu\frac{\partial^3 I(t)}{\partial t^3} \star \int_{V_s} d\mathbf{r}'\ \delta\big[t - \tau(\mathbf{r}_i,\mathbf{r}',\mathbf{r}_j)\big]\ A_{yx}(\mathbf{r}_i,\mathbf{r}',\mathbf{r}_j)\ \delta\epsilon(\mathbf{r}') - \mu\frac{\partial^2 I(t)}{\partial t^2} \star \int_{V_s} d\mathbf{r}'\ \delta\big[t - \tau(\mathbf{r}_i,\mathbf{r}',\mathbf{r}_j)\big]\ A_{yx}(\mathbf{r}_i,\mathbf{r}',\mathbf{r}_j)\ \delta\sigma(\mathbf{r}'), \tag{47}$$

where $\star$ indicates a temporal convolution. The delta functions collapse the spatial integrals over $\mathbf{r}'$ to points that satisfy the travel-time contraint:

$$\{\mathbf{r}' : \tau(\mathbf{r}_i,\mathbf{r}',\mathbf{r}_j) = \tau(\mathbf{r}_i,\mathbf{r}') + \tau(\mathbf{r}',\mathbf{r}_j) = t\}. \tag{48}$$

This locus of points will generally be a curved surface, determined by the velocity in the background model and the positions of the antennas. For example, when transmitter and receiver are coincident in a homogeneous background medium $\mathbf{r}_i = \mathbf{r}_j$, the scattered field at successive times t involves weighted integrals of conductivity and permittivity over larger and larger spherical surfaces,

$$S = \{\mathbf{r}' : 2|\mathbf{r}_j - \mathbf{r}'|/c = t\}.$$

SAR Imaging by Inversion of the GRT

An approximate inversion of equation (47) can be derived by localizing the inversion formula for the ordinary Radon transform over planes.[2] In fact, it is easiest to develop this formula working with equation (43) and the spatial Fourier transformation in spherical coordinates. Our convention for the forward transformation is

$$\tilde{f}(\boldsymbol{\kappa}) = \tilde{f}(\kappa,\hat{\xi}) = \int d\mathbf{r}'\, e^{i\boldsymbol{\kappa}\cdot\mathbf{r}'}\; f(\mathbf{r}') = \int d\mathbf{r}'\, e^{i\kappa\hat{\xi}\cdot\mathbf{r}'}\; f(\mathbf{r}'), \tag{49}$$

where the position vector in the Fourier domain is represented by 3-D spherical coordinates, $\boldsymbol{\kappa} = \kappa\hat{\xi}$; $\hat{\xi}$ is a (radial) unit vector; and κ is the distance from the origin. The inverse transformation is

$$f(\mathbf{r}) = \frac{1}{16\pi^3}\int d\hat{\xi}\int_{-\infty}^{\infty} d\kappa\,\kappa^2 e^{-i\kappa\hat{\xi}\cdot\mathbf{r}}\,\tilde{f}(\kappa,\hat{\xi}), \tag{50}$$

where the $\hat{\xi}$ integral is over the unit sphere. (An extra factor of $1/2$ appears in this formula compared to the standard Cartesian formula because integration over the full unit sphere and over positive and negative radial frequencies κ gives a double coverage of Fourier space.)

In standard spherical coordinates with polar angle θ and azimuthal angle ϕ,

$$\hat{\xi} = (\sin\theta\cos\phi, \sin\theta\sin\phi, \cos\theta)$$

, and $d\hat{\xi} = \sin\theta\, d\phi d\theta$. Substituting (49) into (50) gives

$$f(\mathbf{r}) = \frac{1}{16\pi^3}\int d\hat{\xi}\int_{-\infty}^{\infty} d\kappa\,\kappa^2 \int d\mathbf{r}'\, e^{-i\kappa\hat{\xi}\cdot(\mathbf{r}-\mathbf{r}')} f(\mathbf{r}') \tag{51}$$

Inversion of equation (43) involves reworking it into a form that resembles (51). First, let

$$\mathbf{D}(\mathbf{r}_i,\mathbf{r}_j,\omega) \equiv \begin{pmatrix} D_{xx} \\ D_{yx} \\ D_{xy} \\ D_{yy} \end{pmatrix} \quad \text{and} \quad \mathbf{A}(\mathbf{r}_i,\mathbf{r}_j,\omega) \equiv \begin{pmatrix} A_{xx} \\ A_{yx} \\ A_{xy} \\ A_{yy} \end{pmatrix} \tag{52}$$

be the data and amplitude vectors made from components of the data matrix $\widetilde{\mathbf{D}}$ (equation 33) and the amplitude dyadic $\widetilde{\mathbf{A}}$. In GPR surveys with just horizontal antennas, equation (43) then becomes

$$\mathbf{D}(\mathbf{r}_i,\mathbf{r}_j,\omega) = H(\omega)\int d\mathbf{r}'\; \mathbf{A}(\mathbf{r}_i,\mathbf{r}',\mathbf{r}_j)\; e^{i\omega\tau(\mathbf{r}_i,\mathbf{r}',\mathbf{r}_j)}\; \delta\bar{\epsilon}(\mathbf{r}'), \tag{53}$$

where $H(\omega) = i\mu^2\omega^3 I(\omega)$ is a (pure) frequency factor. Next, assume that the contrast function is localized around an arbitrary point $\mathbf{r}$ and that $\mathbf{A}(\mathbf{r}_i,\mathbf{r}',\mathbf{r}_j)$ varies slowly near $\mathbf{r}$,

$$\mathbf{A}(\mathbf{r}_i,\mathbf{r}',\mathbf{r}_j) \approx \mathbf{A}(\mathbf{r}_i,\mathbf{r},\mathbf{r}_j) + \nabla\mathbf{A}\cdot(\mathbf{r}'-\mathbf{r}) \approx \mathbf{A}(\mathbf{r}_i,\mathbf{r},\mathbf{r}_j), \tag{54}$$

so that it can be approximated by its value at $\mathbf{r}$ and removed from the integral. Multiplying equation (43) by $e^{-i\omega\tau(\mathbf{r}_i,\mathbf{r},\mathbf{r}_j)}$ then gives

$$e^{-i\omega\tau(\mathbf{r}_i,\mathbf{r},\mathbf{r}_j)}\mathbf{D}(\mathbf{r}_i,\mathbf{r}_j,\omega) = H(\omega)\mathbf{A}(\mathbf{r}_i,\mathbf{r},\mathbf{r}_j)\int d\mathbf{r}' e^{i\omega[\tau(\mathbf{r}_i,\mathbf{r},\mathbf{r}_j)-\tau(\mathbf{r}_i,\mathbf{r}',\mathbf{r}_j)]}\,\delta\bar{\epsilon}(\mathbf{r}) \;+\; \text{error} \tag{55}$$

where the "error" term absorbs all the approximations leading to this point.

The right-hand side of equation (55) has the form of a Fourier integral operator acting on the function $\delta\bar{\epsilon}$ (Beylkin, 1985). Its dominant action at $\mathbf{r}$ as $\omega\to\infty$ can be obtained from the first term of a Taylor expansion of the phase about $\mathbf{r}$,

$$\tau(\mathbf{r}_i,\mathbf{r}',\mathbf{r}_j) - \tau(\mathbf{r}_i,\mathbf{r},\mathbf{r}_j) \approx \nabla\tau(\mathbf{r}_i,\mathbf{r},\mathbf{r}_j)\cdot\left(\mathbf{r}'-\mathbf{r}\right). \tag{56}$$

For any given source-receiver pair, the gradient of the total traveltime (on the right-hand side) is the sum of the gradients of traveltimes from the source to point $\mathbf{r}$ and from point $\mathbf{r}$ to the receiver:

$$\nabla\tau(\mathbf{r}_i,\mathbf{r},\mathbf{r}_j) = \nabla\tau(\mathbf{r}_i,\mathbf{r}) + \nabla\tau(\mathbf{r},\mathbf{r}_j). \tag{57}$$

The geometry of this vector relationship is shown in Figure 10. Since traveltime increases as $\mathbf{r}$ moves locally away from the source or receiver along a raypath, $\nabla\tau(\mathbf{r},\mathbf{r}_j)$ points along the ray that arrives at $\mathbf{r}$ from the transmitter; similarly, $\nabla\tau(\mathbf{r}_i,\mathbf{r})$ points along the ray that arrives at $\mathbf{r}$ from the receiver. Let $\hat{\xi}$ be a unit vector in the direction of the total gradient. It is easy to see geometrically or algebraically that

$$\begin{aligned}\nabla\tau(\mathbf{r}_i,\mathbf{r},\mathbf{r}_j) &= \frac{2\cos\alpha(\mathbf{r}_i,\mathbf{r},\mathbf{r}_j)}{c(\mathbf{r})}\,\hat{\xi}(\mathbf{r}_i,\mathbf{r},\mathbf{r}_j) \\ &\equiv s(\mathbf{r}_i,\mathbf{r},\mathbf{r}_j)\hat{\xi}(\mathbf{r}_i,\mathbf{r},\mathbf{r}_j),\end{aligned} \tag{58}$$

where $s \equiv |\nabla\tau| = 2\cos\alpha/c$, and α is half the angle between the two rays at $\mathbf{r}$. The unit vector $\hat{\xi}$ will play the role of the Fourier-domain radial vector in the inversion of equation (55) (by comparison with equation 51). This unit vector is connected to the source and the receiver by the raypaths (Figure 2); thus, integration over $\hat{\xi}(\mathbf{r}_i,\mathbf{r},\mathbf{r}_j)$ becomes an integral over source and receiver positions.

Substituting (58) into (55) gives

$$e^{-i\omega\tau(\mathbf{r}_i,\mathbf{r},\mathbf{r}_j)}\mathbf{D}(\mathbf{r}_i,\mathbf{r}_j,\omega) = H(\omega)\mathbf{A}(\mathbf{r}_i,\mathbf{r},\mathbf{r}_j)\int d\mathbf{r}' e^{i\omega s\hat{\xi}\cdot(\mathbf{r}'-\mathbf{r})}\delta\bar{\epsilon}(\mathbf{r}') \;+\; \text{error} \tag{59}$$

where for simplicity we have dropped the arguments of s and $\hat{\xi}$. The integral term on the right-hand side now resembles the inversion formula (51). But since both sides of this equation are vectors, it is an overdetermined system for the scalar $\delta\bar{\epsilon}$. Least-squares solution of this system amounts to operating on it with the pseudo-inverse of the vector $\mathbf{A}$,

$$\mathbf{A}^{+}(\mathbf{r}_i, \mathbf{r}, \mathbf{r}_j) = \lim_{\varepsilon \to 0} \left(\mathbf{A}^H \cdot \mathbf{A} + \varepsilon \right)^{-1} \mathbf{A}^H, \qquad (60)$$

where ε is a real positive number and the superscript H stands for the Hermitian transpose (to account for a possibly complex amplitude factor). Left-multiplying (59) by $\mathbf{A}^{+}$ and splitting $\delta\bar{\epsilon}$ into components gives

$$\begin{aligned} & e^{-i\omega\tau(\mathbf{r}_i,\mathbf{r},\mathbf{r}_j)} \mathbf{A}^{+}(\mathbf{r}_i, \mathbf{r}, \mathbf{r}_j, \mathbf{u}_j) \cdot \mathbf{D}(\mathbf{r}_i, \mathbf{r}_j, \omega) \\ & \quad = H(\omega) \int d\mathbf{r}' \, e^{i\omega s\hat{\xi}\cdot(\mathbf{r}-\mathbf{r}')} \left[\delta\epsilon(\mathbf{r}') + (-i\omega)^{-1} \delta\sigma(\mathbf{r}') \right] \; + \; \text{error} \\ & \quad . \end{aligned} \qquad (61)$$

Comparing equations (51) and (61) indicates that the final step in the inversion must involve an integral over $\hat{\xi}$ and frequency ω.

If the experiement surrounds the scatterer—e.g., if antenna positions cover a sphere that contains the unknown object—then it is easy to show that both positive and negative spatial frequencies of the object can be recovered from data at positive temporal frequencies ω by the mapping $\boldsymbol{\kappa} = \omega s\hat{\xi}$ (see inset in Figure 10). In practice, because the data must be real, positive temporal frequencies are the only ones available (the data at positive and negative temporal frequencies are complex conjugates). Still, with complete coverage of the Fourier domain, it is possible to reconstruct both $\delta\sigma$ and $\delta\epsilon$ independently, as the real and imaginary parts of the complex function $\delta\bar{\epsilon}$. In effect, probing from both sides of the object gives both positive and negative spatial frequencies. In typical GPR surveys, of course, the object lies in a halfspace and can only be probed from one side. In this geometry only positive spatial frequencies of the object can be reconstructed, and independent recovery of the conductivity and the permittivity perturbations is not possible without further assumptions. We thus consider two separate operators: one recovers the permittivity when the conductivity perturbation is negligible; the other recovers the conductivity when the permittivity perturbation in negligible.

Neglecting $\delta\sigma$ first, consider the linear operator on $\mathbf{D}$,

$$\begin{aligned} \mathcal{H}_\epsilon(\mathbf{D}) = & \frac{1}{16\pi^3} \int d\hat{\xi} \, s^3(\mathbf{r}_i, \mathbf{r}, \mathbf{r}_j) \cdot \\ & \int_{-\infty}^{\infty} d\omega \, \omega^2 H^{-1}(\omega) e^{-i\omega\tau(\mathbf{r}_i,\mathbf{r},\mathbf{r}_j)} \mathbf{A}^{+}(\mathbf{r}_i, \mathbf{r}, \mathbf{r}_j) \cdot \mathbf{D}(\mathbf{r}_i, \mathbf{r}_j, \omega) \end{aligned} \qquad (62)$$

Using equation (51) and (61) (with $\delta\sigma = 0$) gives

$$\begin{aligned} \mathcal{H}_\epsilon(\mathbf{D}) \; &= \; \frac{1}{16\pi^3} \int d\hat{\xi} \, s^3 \int_{-\infty}^{\infty} d\omega \, \omega^2 e^{i\omega s\hat{\xi}\cdot(\mathbf{r}-\mathbf{r}')} \, \delta\epsilon(\mathbf{r}') \; + \; \text{error} \\ &= \; \frac{1}{16\pi^3} \int d\hat{\xi} \; \int_{-\infty}^{\infty} d\kappa \, \kappa^2 e^{i\kappa\hat{\xi}\cdot(\mathbf{r}-\mathbf{r}')} \, \delta\epsilon(\mathbf{r}') \; + \; \text{error} \\ &= \; \langle \delta\epsilon(\mathbf{r}) \rangle \, , \end{aligned} \qquad (63)$$

where the angle brackets indicate an estimate of the quantity. The second equality above follows from the change of variable $\kappa = s\omega$. The frequency factor in $\mathcal{H}_\epsilon$ (equation 62), $\omega^2 H^{-1}(\omega) = [\mu^2 i\omega I(\omega)]^{-1}$, deconvolves the spectrum of the time-derivative of the transmitter current. In practice, the spectrum is not be broadband and the deconvolution must be regularized.

The operator for recovering $\delta\sigma$ differs from $\mathcal{H}_\epsilon$ only by the extra frequency factor $(-i\omega)$,

$$\begin{aligned} \mathcal{H}_\sigma(\mathbf{D}) = & -\frac{1}{16\pi^3} \int d\hat{\xi} \, s^3(\mathbf{r}_i, \mathbf{r}, \mathbf{r}_j) \cdot \\ & \int_{-\infty}^{\infty} d\omega \, i\omega^3 H^{-1}(\omega) e^{-i\omega\tau(\mathbf{r}_i,\mathbf{r}',\mathbf{r}_j)} \mathbf{A}^{+}(\mathbf{r}_i, \mathbf{r}, \mathbf{r}_j) \cdot \mathbf{D}(\mathbf{r}_i, \mathbf{r}_j, \omega) \end{aligned} \qquad (64)$$

The frequency factor of this operator removes the spectrum of the transmitter current.

Figure 10 Geometry of rays at image point

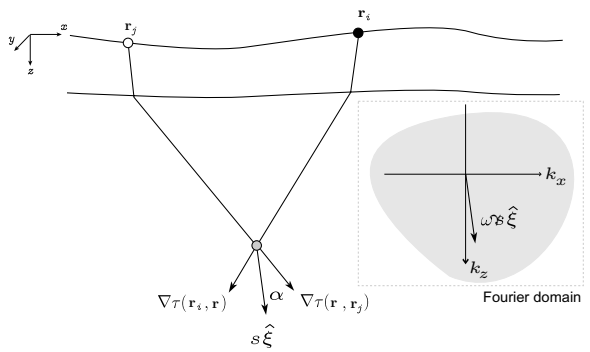

GPR Imaging in a Homogeneous Wholespace

The simplest example of the imaging formula is for a vector radar survey with co-incident pairs of antennas in a homogeneous background medium (this neglects effects at the earth-air interface for a GPR survey). The following geometrical parameters specify the experimental geometry:

$$\begin{aligned} \mathbf{r}_j &= (x_j, y_j, 0), \text{ position vector of the } j\text{-th antenna pair} \\ R &= |\mathbf{r} - \mathbf{r}_j|, \text{ distance from } \mathbf{r}_j \text{ to image point } \mathbf{r}; \\ \hat{\mathbf{R}} &= (\mathbf{r} - \mathbf{r}_j)/R, \text{ unit vector from the antennas to } \mathbf{r}; \\ \theta_{\mathbf{r},\mathbf{r}_j} &= \text{polar angle between } \hat{\mathbf{R}} \text{ and the z-axis, and} \\ \phi_{\mathbf{r},\mathbf{r}_j} &= \text{azimuthal angle between } \hat{\mathbf{R}} \text{ and the } x\text{-axis,} \end{aligned}$$

Then, from equation (42), the amplitude vector $\mathbf{A}$ splits into a scalar amplitude that depends on R and a projection vector $\mathbf{P}$ that depends on only the angles $\theta_{\mathbf{r},\mathbf{r}_j}$ and $\phi_{\mathbf{r},\mathbf{r}_j}$,

$$\mathbf{A}(\mathbf{r}_i,\mathbf{r},\mathbf{r}_j) = A(R)\,\mathbf{P}(\theta_{\mathbf{r},\mathbf{r}_j},\phi_{\mathbf{r},\mathbf{r}_j}), \tag{65}$$

where

$$\begin{aligned} P_{xx} &= \hat{\mathbf{x}}\cdot(\widetilde{\mathbf{I}}-\hat{\mathbf{R}}\hat{\mathbf{R}})\cdot\hat{\mathbf{x}} = 1-\sin^2\theta_{\mathbf{r},\mathbf{r}_j}\cos^2\phi_{\mathbf{r},\mathbf{r}_j} \\ P_{yy} &= \hat{\mathbf{y}}\cdot(\widetilde{\mathbf{I}}-\hat{\mathbf{R}}\hat{\mathbf{R}})\cdot\hat{\mathbf{y}} = 1-\sin^2\theta_{\mathbf{r},\mathbf{r}_j}\cos^2\phi_{\mathbf{r},\mathbf{r}_j} \\ P_{yx} = P_{xy} &= \hat{\mathbf{y}}\cdot(\widetilde{\mathbf{I}}-\hat{\mathbf{R}}\hat{\mathbf{R}})\cdot\hat{\mathbf{x}} = \sin^2\theta_{\mathbf{r},\mathbf{r}_j}\cos\phi_{\mathbf{r},\mathbf{r}_j}\sin\phi_{\mathbf{r},\mathbf{r}_j}, \end{aligned}$$

and

$$A = \frac{1}{16\pi^2}\frac{e^{-\sigma\mu cR}}{R^2},$$

A straightforward calculation shows that $\mathbf{A}^H\cdot\mathbf{A} = A^2(1+\cos^4\theta_{\mathbf{r},\mathbf{r}_j})$. For this geometry, the incident and scattered rays point in the same direction: $\alpha = 0$, $s = 2/c$, and $\hat{\xi} = \hat{\mathbf{R}}$. The integration over $\hat{\xi}$ is easily converted to an integral over the antenna positions (Miller et al., 1987) with

$$d\hat{\xi} = \cos\theta_{\mathbf{r},\mathbf{r}_j}/R^2\; d\mathbf{r}_j.$$

Finally, $P^H = P^T$ since the projection factors are real. Putting this all together gives

$$\begin{aligned} \langle\delta\epsilon(\mathbf{r})\rangle &= \frac{8}{\pi c^3\mu^2}\int d^2\mathbf{r}_j\frac{\cos\theta_{\mathbf{r},\mathbf{r}_j}}{1+\cos^4\theta_{\mathbf{r},\mathbf{r}_j}}\cdot \\ &\int_{-\infty}^{\infty} d\omega\,\frac{1}{i\omega I(\omega)}e^{-2i\omega R/c}\,\mathbf{P}^T(\theta_{\mathbf{r},\mathbf{r}_j},\phi_{\mathbf{r},\mathbf{r}_j})\cdot\mathbf{D}(\mathbf{r}_j,\omega)e^{\sigma\mu cR} \\ &= \frac{4}{c^3\mu^2}\int d^2\mathbf{r}_j\frac{\cos\theta_{\mathbf{r},\mathbf{r}_j}}{1+\cos^4\theta_{\mathbf{r},\mathbf{r}_j}}\cdot \\ &\mathbf{P}^T(\theta_{\mathbf{r},\mathbf{r}_j},\phi_{\mathbf{r},\mathbf{r}_j})\cdot\mathbf{D}^*(\mathbf{r}_j,t=2|\mathbf{r}-\mathbf{r}_j|/c)e^{\sigma\mu c|\mathbf{r}-\mathbf{r}_j|}, \end{aligned} \tag{66}$$

where $\mathbf{D}^*(\mathbf{r}_j,t)$ is the data deconvolved by the time-derivative of the transmitter current $\partial I(t)/\partial t$. The exponential amplitude factor corrects for attenuation in the background medium (geometrical spreading is implicitly corrected by the integral over $d\mathbf{r}_j$). In the final formula, we have substituted $R = |\mathbf{r}-\mathbf{r}_j|$, so all geometrical quantities are explicit. The formula for $\delta\sigma$ is the same except that data is first deconvolved by $I(t)$.

In practice, equation (66) is a vector stacking algorithm. Let p index (discrete) image points and ij source-receiver positions, then

$$\begin{aligned} &IMAGE(p) = \\ &\sum_j w_{xx}(p,j)\,D^*_{xx}(j,t(p,j)) + \sum_j w_{yy}(p,j)\,D^*_{yy}(j,t(p,j)) + \\ &\sum_j w_{xy}(p,j)\,D^*_{xy}(j,t(p,j)) \end{aligned} \tag{67}$$

where $D^*_{\bullet\bullet}$ is the data (appropriately filtered), $t(p,j)$ is the (round trip) traveltime to the image point, and the discrete weights $w_{\bullet\bullet}$ absorbs all other factors.

Figure 11 Stepped-time impulse radar

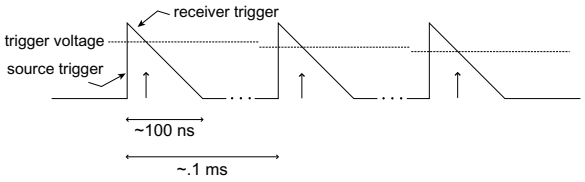

0.1.4. Practical Description

Daniels (1996) gives the most comprehensive description of modern GPR equipment, including both commercial and experimental systems; other general references are Daniels et al. (1988), Peters et al. (1994), and Davis and Annan (1989). Extensive descriptions of systems and their applications are now also available online (a good starting point is `www.g-p-r.com`). The 3 largest commercial manufacturers of general purpose GPRs are:

- Geophysical Survey Systems, Inc.
  `www.geophysical.com`
- Sensors and Software, Inc.
  `www.sensoft.on.ca`
- Malå Geoscience
  `www.malags.se`

The systems currently available from these manufacturers are impulse radars that sample and record waveforms digitially. Inexpensive and rugged analog-to-digital converters (ADCs) do not, however, operate fast enough to cover the broad bandwidth of GPRs, which can be several hundred MHz or more. These systems therefore build up a full transient waveform one sample at a time by firing the source repeatedly and, at each firing, capturing and recording one sample of the waveform at successively increasing time delays. This "stepped-time" recording is a standard method used by fast sampling oscilloscopes: A capacitor is discharged repeatedly to generate broadband impulses at a rate, $f_s = 1/DT_s$, of about 100,000 per second. In synchronization with the source, but with a slightly lower frequency, $f_r = 1/(DT_s+dt)$, a circuit is repeatedly triggered to sample and hold a value proportional to the voltage between the receiver antenna leads at the moment of triggering. If the source is repeatable and the sampling frequencies are stable, this sampling shifts frequencies down by a factor of $(f_s-f_r)/f_r$, converting radio frequencies to audio frequencies and creating a signal that can be digitized by an audio-band digitizer.

A few "stepped-frequency" GPR systems have also been built by specialized manufacturers. These systems operate by broadcasting and coherently detecting one frequency at a time that sweeps through

the GPR bandwidth. In principle, stepped-time and stepped-frequency systems are equivalent through a Fourier Transform, provided the source is perfectly repeatable and the noise is stationary. Of course, neither condition holds exactly.

Digital impulse radars

A generic digital impulse radar uses the following components:

- A trigger generator,
- A source antenna, with associated pulser electronics,
- A receiver antenna, with associated sampling electronics,
- An ADC connected to a storage device (often a laptop computer).

The last three components are all configured to be synchronized by signals from the trigger generator. The trigger system generally works by first generating an accurate and stable sawtooth wave (Figure 11) that repeats at audio frequencies (10-100 kHz) and has a precise $slope = \Delta V/\Delta t$ on its trailing edge. Conceptually, this sawtooth wave itself could be used to synchronize source and receiver electronics. For example, the source can be set to fire at the initial jump of the sawtooth (from 0 to 1), while the receiver electronics can be set to capture and digitize a sample (of the voltage across its antenna leads) when the trailing slope of the sawtooth fails below a certain voltage v_R. Decreasing this receiver trigger voltage by a fraction Δv_R on successive firings delays successive samples in time by $\Delta t = \Delta v_R / slope$.

In practice, separate square-wave triggers for the source and receiver electronics are usually created from the sawtooth using a digital-to-analog convertor and a comparator[3] by a loop of the form:

```
isv=VS
irv=VR0
For is=1:NSAMP
 irv=irv-deltaV_R;
 rtrig=COMP(sawtooth,D2A(irv));
 strig=COMP(sawtooth,D2A(isv));
END
```

In this scheme, the length of the "on" (1) interval in the train of square waves sent to the source electronics has a fixed length, whereas this interval gradually increases in length with each successive wave in the train sent to the receiver electronics. An advantage of sending square waves is that their binary nature can allow more accurate detection of the trigger time. Also, the leading pulse of the square wave ("on") can signal the electronics to prepare for action that is triggered by the trailing edge ("off"). Obviously, any distortion of these trigger pulses can cause a loss of samples or variations in their timing. With modern electronics, however, the timing can be accurate to hundredths of a nanosecond.

Antennas

The antennas of impulse GPRs are generally linear or bow-tie antennas designed to radiate and receive as broadband dipoles (Figure 5). The central frequency of a bow-tie antenna is inversely proportional to its length, so a 250 MHz antenna will be twice as long (and occupy 8 times the volume) as a 500 MHz antenna. (A bow-tie antenna with a spectrum very close to the one shown in Figure 6 has a length of 25 cm.) To minimize ringing, the ends of the antennas are resistively loaded (Shlager, et al., 1994). Antennas in newer systems are also surrounded with radar absorbing material and placed in a rectangular metal cavity to minimize radiation into the air.

The source electronics consist of a capacitor (or cascading set of capacitors) that discharge through avalanche transistors at the trigger signal. Consistency of source signatures depends on the manufacturers' abilities to control variations in the charge and discharge cycle as temperature, moisture, or other environmental factors vary. Most systems need some warmup time before use.

The receiver electronics consists of a sampler whose input leads are connected to the voltage gap in the receiving antenna. When triggered, the sampler voltage jumps to a value proportional to the voltage difference at the gap and holds that value long enough for an ADC operating at kHz frequencies to digitize and record the signal.

Digitization

The voltage sampled at the receiver is not very different from the voltage on an audio microphone. A preamplifier close to the receiver boosts the signal to a level suitable for digitization by an ADC similar to those used for digitizing audio. Depending on the age of the system design, the data will be digitized to an accuracey from twelve to twenty bits. Time-varing gain can be applied before digitization to compensate for limitations in bit length. Gain applied after digitization cannot improve signal-to-noise ratios, but may be part of the digital signal processing chain. The digitized data is generally stored directly to a PC, which is either a dedicated device or a consumer laptop.

Figure 12 Lab Survey Location

0.1.5. Applications and examples

The following examples from the authors' files illustrate cases where 3-D GPR imaging proved useful. The scanning system used in the last two examples was developed in a project on ground-penetrating imaging radar partly funded by the Electric Power Research Institute (EPRI) and the Gas Research Institute (GRI).

Laboratory Floor

In March 1997, the facilities manager at Schlumberger-Doll Research asked if a ground-penetrating radar survey could show structures beneath the floor of lab workshop where a new elevator was being planned. The location is shown in Figure 12. A floor drain just outside the door visible in the figure suggested that pipes might lie under the floor.

We collected 2 multi-polarization 3D GPR surveys using a set of linear-dipole antennas with nominal frequency of 900 MHz. The data were collected with an antenna separation of .17 m, on a regular 2-D grid with an inline sampling rate of one trace every 0.02 m and a crossline sampling of one line every 0.04 m. The rail system visible in Figure 12 was used to guide the equipment and to control the crossline spacing. A string, fixed at one side of the rail, was used to trigger the pulse every 0.02 m. We collected three data sets in which source and receiver dipoles were respectively parallel to each other and perpendicular to the line of acquisition (TE), parallel to each other and parallel to the line of acquisition (TM), and perpendicular to each other (X).

The data were processed using a version of the algorithm in equation 66. Figure 13 shows the image volume rendered in a way to show low-amplitude returns from the near subsurface. The regular grid pattern is understood to be the image of a steel reinforcement mesh.

Figure 13 3D GPR image

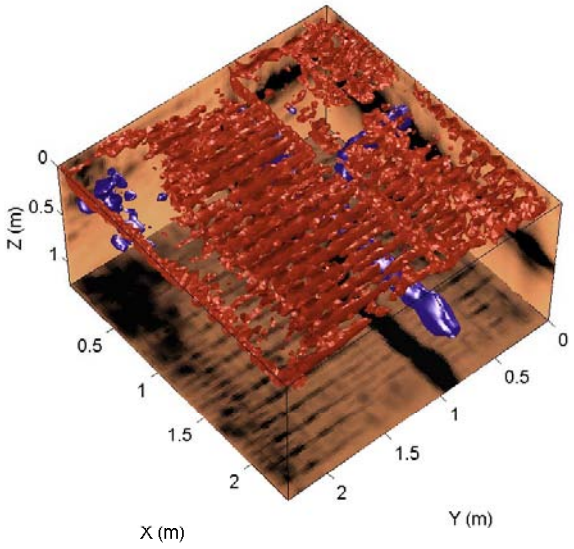

Figure 2 shows the image volume rendered as an isosurface at a relatively high amplitude value. In this display we see a clear image of a pair of pipes joind by a standard 45-degree fitting. Figure 14 shows a horizontal projection of the image, overlain by a copy of the building plans drawn in 1955. The planned pipe location runs through a region where the GPR image shows an anomaly. This anomaly could be caused by bedrock whose presence caused the builders to deviate from the plans.

Figure 14 Projection of GPR image combined with floor plan.

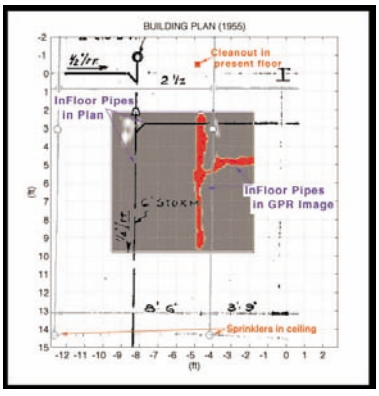

Figure 15 Zone of injection of the barrier

Figure 16 Injection

Injected Colloidal Gel During August 1997 a project organized by Lawrence Berkeley Laboratory was carried out to test the feasibility of controlling buried contaminents by injecting colloidal silica gel to form an impermeable wall around the contaminants. In the test, which took place at Brookhaven National Laboratory, an attempt was made to form a barrier in the form of a half-V with three vertical walls and one wall slanted at 45 degrees. Figure 1 shows the site after the injection of the walls. The four walls are marked in orange, with the slanted wall on the right. The walls are about 10m long and were injected to a depth of 10m deep.

Figure 15 shows the site after the injection of the walls. The four walls are marked in orange, with the slanted wall on the right. The walls are about 10m long and were injected to a depth of 10m deep. Figure 16 shows injection of part of the wall closest to the road. In the injection process, colloidal silica is pumped through a hollow drill stem as it is jackhammered into the sand.

A 3D GPR survey with 100 MHz antennas was acquired after the placement of the slanted wall and the vertical wall closest to the road. Data was collected along 35 scan lines, each with 60 transceiver locations, on a one foot grid starting at the slanted wall. Figure 17 shows the acquistion.

Figure 18 shows the reconstructed 3D image volume. Figure 20 is a composite of views into the image. After some shallow slightly dipping events are clipped from view the dipping "wall" is visible as a sequence of blobs, one of which has a kink in it that makes it discontinuous with its neighbors below about 5 ft.

Figure 17 GPR acquisition

Figure 18 3D GPiR Image of injected gel

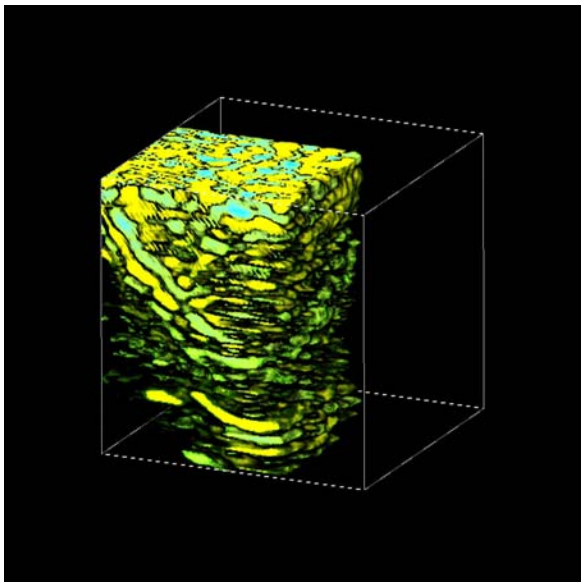

Figure 20 3D images of gel

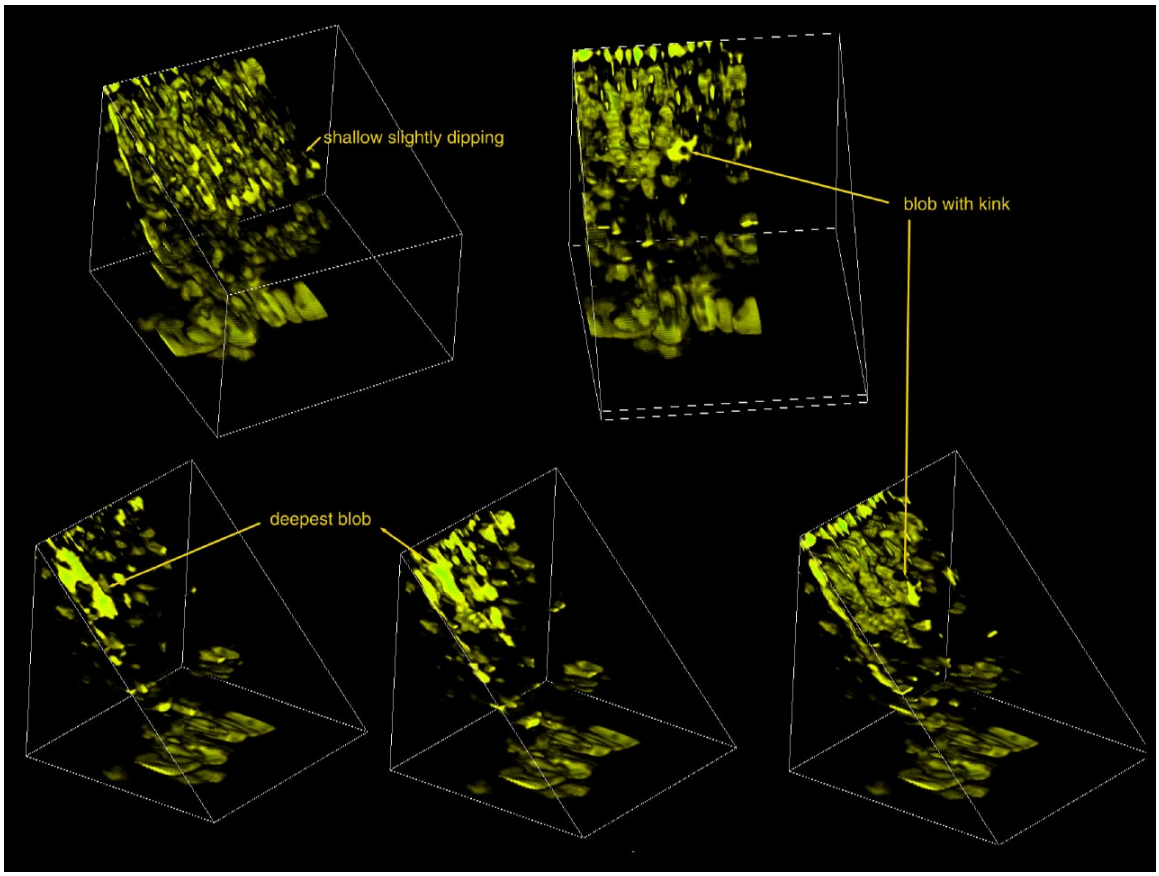

Figure 19 Survey at rock quarry

Monitoring fluids in a porous rock

In 1999 a survey was made at a rock quarry in Portland, Connecticut, to test if time-lapse 3D GPiR could monitor the flow of fluid injected into a porous rock. Figure 19 shows the setup: Two pairs of 400 MHz antennas ("A" in Figure 19) were scanned on a motorized, computer-controlled frame over a .05 m grid covering an area roughly 2.5 m by 2.5 m. A borehole 3 m long ("B" in Figure 19) was drilled at an oblique angle to the scan directions. During a two-hour period, eight surveys were made while saline brine was injected into the rock from the packed-off end of the borehole. Data from a baseline survey were subtracted from each successive survey and a series of 3-D images were created.

Figure 21 shows frames taken at 20, 50, and 80 minutes after start of the injection. The left panel shows the frames in 3-D perspective; the right panel shows the same images projected onto a photograph of the rock surface. The borehole was imaged independently and appears in red in the left panel, yellow in the right panel. It is evident that the fluid found its way to a high-permeability bedding surface within the sandstone and flowed mainly toward the rock face lying at the right edge of the images in

Figure 21 GPiR images at 30 minute intervals

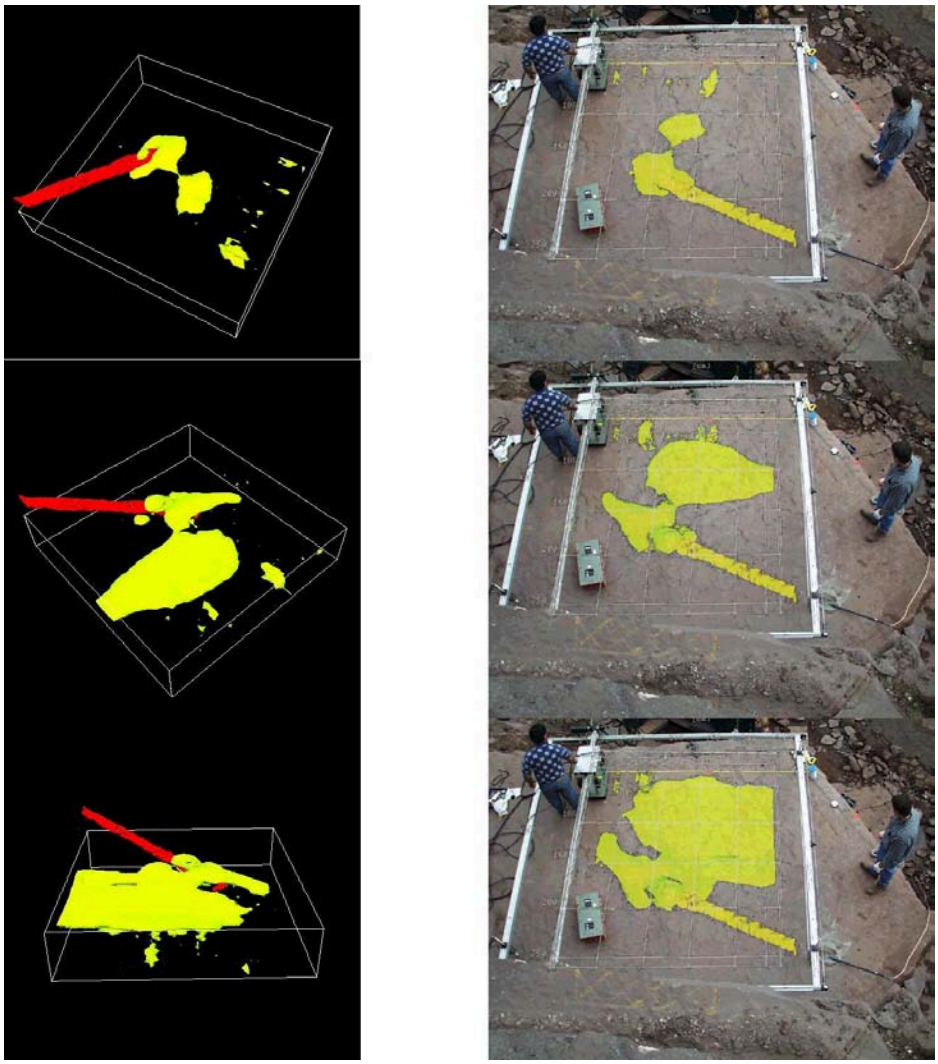

Figure 21. Figure 22 show a photo of the brine as it emerged from the rock. An arrow marks the location where the first fluid emerged. It lies directly in line with the flow seen in Figure 22.

Figure 22 Injected fluid emerging from rock

0.1.6. Acknowledgements

Notes

1. Accuracy of the Born and related approximations, such as the Rytov approximation, are the subject of a large and controversial literature (see, e.g., Oristaglio, 1985). It is difficult to state precisely all the condtions under which the Born approximation is accurate, but it is certainly accurate under the condition that the scattered field is small (pointwise) compared to the incident field inside the scattering volume.
2. Norton and Linzer (1978) first derived a scalar version of equation (47) for pulse-echo imaging (medical ultrasound) in a homogeneous background medium and recognized its connection with the generalized Radon transform over spheres. They derived an exact inversion formula for this specific GRT in the spatial Fourier transform domain. Miller et al. (1987) developed the general form of this equation for acoustic imaging and derived a simple approximate inversion formula by localizing the formula for inversion of the standard Radon transform. Beylkin (1985) provided a justification for this approximate formula through the theory of Fourier Integral Operators.
3. A comparator, COMP(a,b), is a component that gives an output voltage equal 1 when $a > b$, 0 otherwise

References

1. Beylkin, G., 1985, Imaging of discontinuities in the inverse scattering problem by inversion of a causal generalized Radon transform, *J. Math. Phys.*, **26**, 99–108.
2. Buderi, R., 1996, *The Invention that Changed the World*, Simon and Schuster.
3. Born, M., and Wolf, E., 1999, *Principles of Optics*, 7th ed., Cambridge U. Press.
4. Chew, W., 1990, *Waves and Fields in Inhomogeneous Media*, Van Nostrand, New York.
5. Claerbout, J.F., 1976, *Fundamentals of Geophysical Data Processing*, McGraw-Hill, New York.
6. Daniels, D. J., 1996, *Surface-Penetrating Radar*: Institution of Electrical Engineers, London.
7. Deans, S. R., 1983, *The Radon transform and some of its applications*, J. Wiley & Sons, New York.
8. Daniels, D.J., Gunton, D.J., and Scott, H.F., 1988, Introduction to subsurface radar, *IEE Proc.*, **135**, 278–320.
9. Davis, J.L., and Annan, A.P., 1989, Ground-penetrating radar for high-resolution mapping of soil and rock stratigraphy: *Geophys. Prospect.*, **37**, 531–551.
10. Engheta, N., and Papas, C.H., 1982, Radiation patterns of interfacial dipole antennas: *Radio Science*, **17**, 1557–1566.
11. Felsen, L., and Marcuvitz, N., 1973, *Radiation and Scattering of Waves*, Prentice-Hall.
12. Helgason, S., 1984, *Groups and geometric analysis: Integral geometry, invariant differential forms, and spherical functions*, Academic Press.
13. Hipp, J. E., 1974, Soil electromagnetic parameters as functions of frequency, soil density, and soil moisture: *Proc. IEEE*, **62**, 98–103.
14. Kline, M., and Kay, M., 1965, *Electromagnetic theory and geometrical optics*, Krieger.
15. Kraus, J. D., 1988, *Antennas*, 2nd ed., McGraw-Hill.
16. Luebbers, R., Hunsberger, F.P., Junz, K.S., Standler, R.B., and Schneider, M., 1990, A frequency-dependent finite-difference time-domain formulation for dispersive materials: *IEEE Trans. Electromag. Compat.*, **32**, 222–227.
17. Miller, D., Oristaglio, M., and Beylkin, G., 1987, A new slant on seismic imaging: Migration and integral geometry, *Geophysics*, **53**, 943–964.
18. Oristaglio, M. L., 1985, Accuracy of the Born and Rytov approximations for the case of refraction and reflection at a plane interface, *J. Optical Soc. America A, Optics and Image Science*, **2**, 1987–1993.
19. Nishioka, Y., Maeshima, O., Uno, T., and Adachi, S., 1999, Three-dimensional FDTD analysis of resistor-loaded bow-tie antennas covered with ferrite-coated conducting cavity for subsurface radar, *IEEE Trans. Ant. Propagat.*, **47**, 970–977.
20. Norton, S.G., and Linzer, M., 1981, Ultrasonic scattering potential imaging in three dimensions: Exact inverse scattering algorithms for plane, cylindrical, and spherical apertures, *IEEE Trans. Biomed. Eng.*, **BME-28**, 202–220.
21. Peters, L., Jr, Daniels, J. J., and Young, J. D., 1994, Ground penetrating radar as a subsurface environmental sensing tool: *Proc. IEEE*, **82** (Special Issue on Remote Sensing of the Environment), 1802–1822.
22. Shlager, K.L., Smith, G.S., and Maloney, J.G., 1994, Optimization of bow-tie antennas for pulse radiation, *IEEE Trans. Ant. Propagat.*, **42**, 975–982.
23. Skolnik, M. I., 1980, *Introduction to radar systems*, 2nd ed., McGraw-Hill.
24. Wang, T., and Oristaglio, M., 2000, Simulation of GPR surveys over pipes in dispersive soils, to appear in *Geophysics*.
25. Wang, T., and Oristaglio, M., 2000, GPR imaging by generalized Radon transform, to appear in *Geophysics*.